Electronic Supplementary Material (ESI) for Journal of Materials Chemistry A.

Supporting Information

Design and Synthesis of Integrally Structured Ni_3N Nanosheets/Carbon Microfibers/Ni_3N Nanosheets for the Efficient Full Water Splitting Catalysis

Tingting Liu,[a] Mian Li,[a] Chuanlai Jiao,[a] Mehboob Hassan,[a] Xiangjie Bo,*[a] Ming Zhou,*[a] and Hsing-Lin Wang*[b]

[a] *Key Laboratory of Nanobiosensing and Nanobioanalysis at Universities of Jilin Province, Key Laboratory of Polyoxometalate Science of Ministry of Education, and National & Local United Engineering Laboratory for Power Batteries, Department of Chemistry, Northeast Normal University, Changchun, Jilin Province 130024, P. R. China. E-mail: baoxj133@nenu.edu.cn; zhoum739@nenu.edu.cn*

[b] *Department of Materials Science & Engineering, Southern University of Science & Technology, Shenzhen, Guangdong 518055, P.R. China. E-mail: wangxl3@sustc.edu.cn*

1. Experimental Section

1.1. Reagents

Hexamethylenetetramine (HMT), nickel acetate, Nafion solution (5 wt%), KOH, absolute ethyl alcohol, and carbon nanotubes (CNTs) were purchased from Aladdin. NH_3 was purchased from Juyang Gas Company, Changchun, China. All other reagents were analytical grade and without further purification.

1.2. Synthesis of the carbon matrix of GO, CNTs, MPCs and CMFs

The GO was synthesized from primary graphite particles by the Hummer's method.[1] CNTs was washed with 68 wt% HNO_3 solution at 120 ℃ for 12 h to open their ends and activate the surfaces. After being washed with deionized water to neutral state, the CNTs were dried at 80 ℃ in oven. MPCs was synthesized by previous method,[2] in which the commercial hydrophilic nano-$CaCO_3$ and sucrose act as template and act carbon precursor, respectively. CMFs were derived from forwards collected biomass (catkins) as reported previously by us.[3]

1.3. Synthesis of the Ni-based precursors for Ni_3N-CNTs, Ni_3N-Gr, Ni_3N-MPCs, Ni_3N/CMFs/Ni_3N and bulk Ni_3N

The detailed synthetic route for producing the Ni-based precursor of Ni_3N/CMFs/Ni_3N (Ni_3N-CNTs, Ni_3N-Gr or Ni_3N-MPCs) was summarized in **Scheme 1**. In details, 120 mg of the carbon matrix of CMFs (CNTs, GO or MPCs), 2 mM nickel acetate and 4 mM HMT were dissolved in 40 mL of distilled water under vigorous stirring for 2 h to form the uniform mixture slurries. Then, the as-prepared mixture slurries were thoroughly transferred into the 60 mL Teflon-lined autoclaves and heated at 120 ℃ for another 12 h. After they were cooled down to room temperature, the final product was collected after centrifuging the resultant mixture solution. Finally, the Ni-based precursor of Ni_3N/CMFs/Ni_3N (Ni_3N-CNTs, Ni_3N-Gr, or Ni_3N-MPCs) was obtained after the product was washed (with water and ethanol) for several times and dried in a vacuum overnight.

The precursor of bulk Ni_3N was synthesized by the procedure being similar to that of the Ni_3N/CMFs/Ni_3N. The only difference is that no carbon matrix was added into the mixture slurries before they were kept in the 60 mL Teflon-lined autoclaves.

1.4. Synthesis of the hybrid materials of Ni_3N-CNTs, Ni_3N-Gr, Ni_3N-MPCs, Ni_3N/CMFs/Ni_3N, bulk Ni_3N and NiO-CMFs

To synthesize the hybrid material of Ni_3N/CMFs/Ni_3N (Ni_3N-CNTs, Ni_3N-Gr or Ni_3N-MPCs), the as-prepared Ni-based hybrid precursor of Ni_3N/CMFs/Ni_3N (Ni_3N-CNTs, Ni_3N-Gr or Ni_3N-MPCs) was placed in porcelain boats in the tube furnace and then heated to 400 ^oC with a heating rate of 5 ℃ min^{-1} under the NH_3 atmosphere. After keeping the temperature of 400 ^oC for 2 h, the system was naturally cooled down to room temperature under the NH_3 atmosphere. The black product of Ni_3N/CMFs/Ni_3N (Ni_3N-CNTs, Ni_3N-Gr or Ni_3N-MPCs) was collected for further characterization and test.

To get the NiO/CMFs/NiO hybrid composite, the precursor of Ni_3N/CMFs/Ni_3N was placed in the tube furnace and then heated to 400 ℃ at a rate of 5 ℃ min^{-1} under the air atmosphere. After

keeping the temperature of 400 ^{o}C for 2 h, the system was naturally cooled down to room temperature under the air atmosphere. Then the as-prepared product of NiO/CMFs/NiO was collected for further characterization and test.

To synthesize the bulk Ni_3N, the precursor of bulk Ni_3N was also placed in porcelain boats in the tube furnace and then heated to 400 ^{o}C with a heating rate of 5 ℃ min^{-1} under the NH_3 atmosphere.

Finally, in order to study the influence of nitridation temperatures on the OER/HER catalysis performances of different Ni_3N/CMFs/Ni_3N-*T* (*T* values indicate the pyrolysis temperatures) samples. The as-prepared Ni-based hybrid precursors of Ni_3N/CMFs/Ni_3N was calcined at *T*=350, 400, 450, 500, and 550 ^{o}C with a heating rate of 5 ℃ min^{-1} under the NH_3 atmosphere. For all samples appeared in this paper, without special illustration, all samples were heated at 400 ^{o}C.

1.5. Physical characterization of resultant catalysts.

Wide-angle XRD patterns were obtained on an X-ray D/max-2200 vpc (Rigaku Corporation, Japan) instrument operated at 40 kV and 20 mA using Cu Kα radiation (*k* 0.15406 nm). SEM images were performed using a Philips XL-30 ESEM equipped with an EDX analyzer. TEM analysis was performed on a high-resolution Hitachi JEM-2100 system. Surface chemical analyses of resultant catalysts were carried out by XPS on an ESCA LAB spectrometer (USA) using a monochromatic Al Kα source (*hv* 1486.6 eV). The binding energies were calibrated by using the containment carbon (C1s 284.6 eV). The N_2 adsorption-desorption isotherms were performed on an ASAP 2020 (Micromeritics, USA). Before the measurements, the samples were degassed in vacuum at 150 ℃ for 6 h. The Brunauer-Emmett-Teller (BET) method was utilized to calculate the BET specific surface area using adsorption data. The pore size distribution was derived from the adsorption branch by using the Barrett-Joyner-Halenda (BJH) model. Raman spectra were obtained using a confocal microprobe Raman system (HR800, JobinYvon).

1.6. Electrochemical characterization methods

All electrochemical measurements for OER and HER were performed with a standard three-electrode cell at room temperature by using a rotating disk electrode (RDE) modified by catalysts as the working electrode (5 mm in diameter, 0.19625 cm^2). Ag/AgCl was used as reference electrodes and Pt wire was used as counter electrode for OER test. All potentials appeared in this paper are referred to reversible hydrogen electrode (the potentials recorded and referred to reversible hydrogen electrode in each experiment were calculated using the formula $E_{RHE} = E_{Ag/AgCl} + 0.059pH + 0.197$ V, where E_{RHE} is a potential *vs.* reversible hydrogen electrode (*vs.* RHE), $E_{Ag/AgCl}$ is a potential *vs.* Ag/AgCl electrode, and pH is the pH value of electrolyte. All current densities are the ratios of recorded currents to the geometric area of electrode. The onset potentials (E_{onset}) were determined from the intersection of the tangents of OER current and the polarization curve baseline. The resistance of the electrolytes was measured and the linear sweep voltammograms (LSVs) were recorded with *iR* drop compensation unless specifically mentioned.

In order to prepare the working electrodes, 3 mg of catalyst powders were firstly dispersed in 1 mL Nafion solution (0.5 wt%) with 45 min of ultrasonication to generate homogeneous inks. Next, 30 uL of the dispersion was transferred onto the GCE with the catalyst loading amount of 0.306 mg cm^{-2}. Finally, the as-prepared catalyst film was dried at room temperature.

In the electrochemical testing processes for the OER and HER; the polarization curves were plotted as potential (E / V *vs.* RHE) *vs.* log |j / mA cm^{-2}| to get the Tafel plots for assessing the OER kinetics of resultant catalysts. By fitting the linear portion of the Tafel plots to the Tafel equation ($\eta = b \log (j) + a$), the Tafel slope (b values) can be obtained.

For the full water splitting tests, a standard two-electrode cell was adopted. The Ni_3N/CMFs/Ni_3N hybrid samples are used as both negative and positive electrodes to construct the (-) Ni_3N/CMFs/Ni_3N||Ni_3N/CMFs/Ni_3N (+) electrolysis system; for comparation, existing most efficient catalytic benchmark of (-) Pt||RuO_2 (+) was also tested for water splitting reaction.

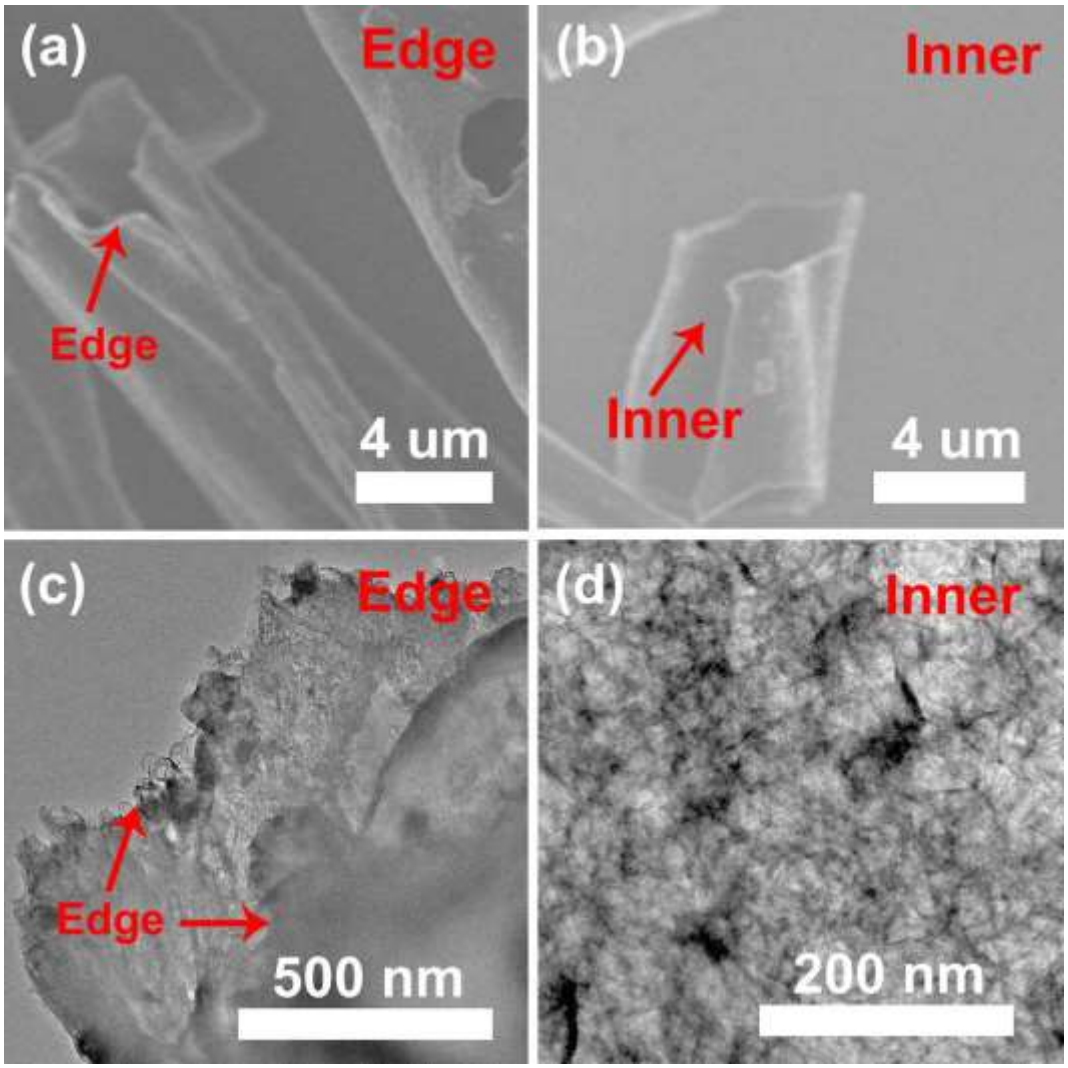

Figure S1 (a and b) SEM images of an individual CMFs. (c) TEM image of the edge part on the outer surface of an individual CMFs. (d) TEM image of the inner surface of an individual CMFs.

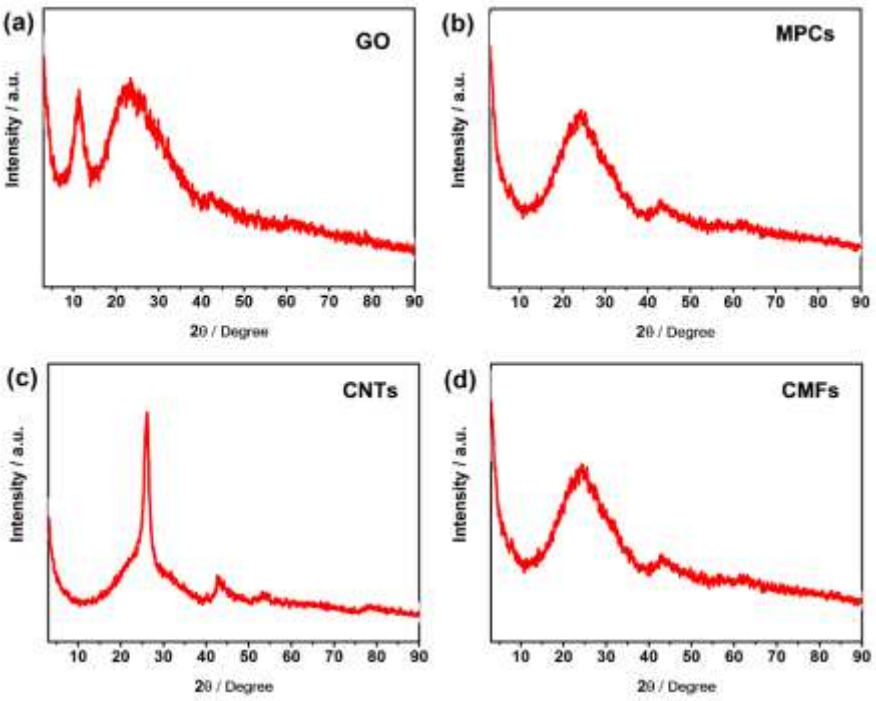

Figure S2 XRD patterns of (a) GO, (b) MPCs, (c) CNTs, and (d) CMFs matrices.

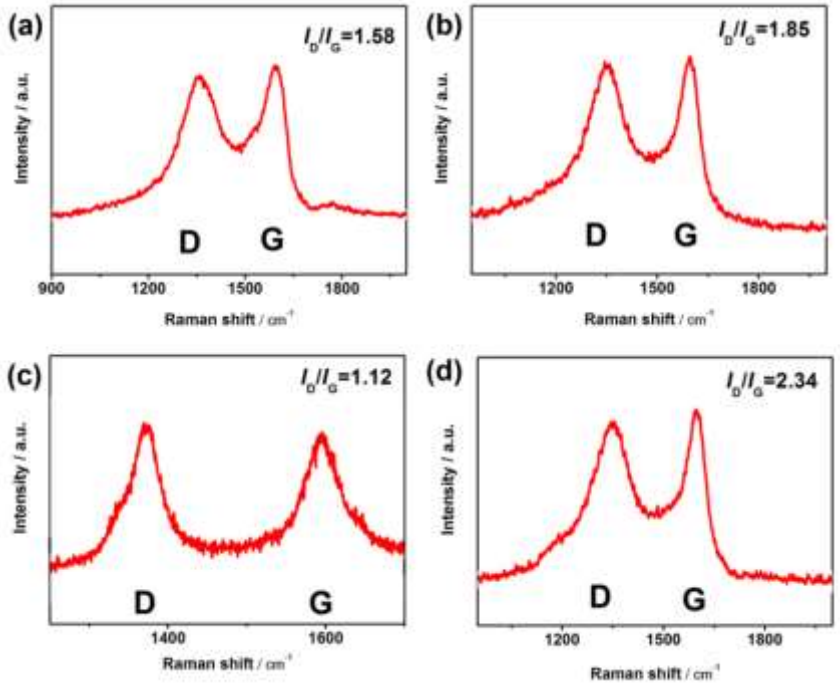

Figure S3 Raman spectra of (a) GO, (b) MPCs, (c) CNTs, and (d) CMFs matrices.

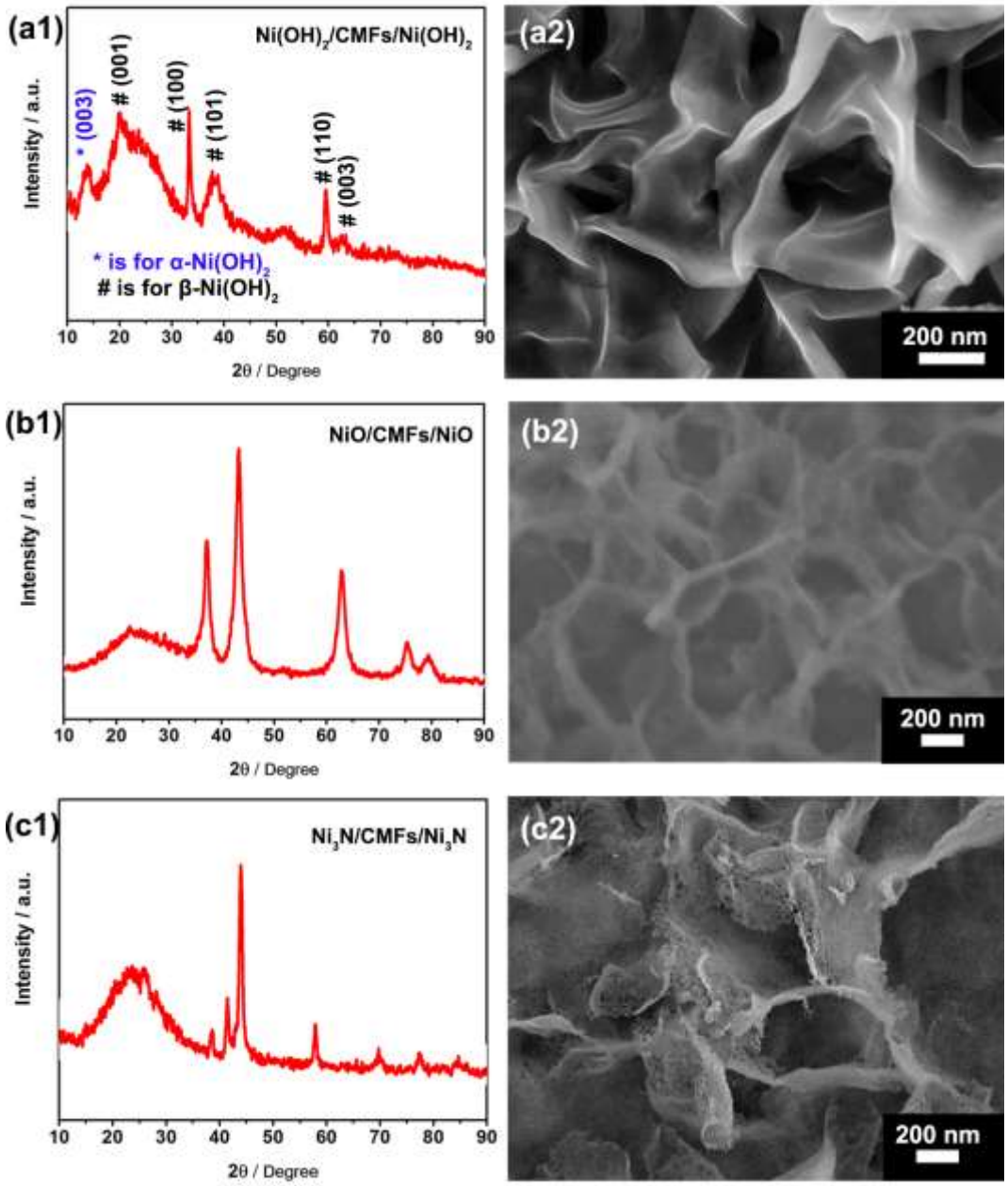

Figure S4 XRD patterns (a1, b1 and c1) and SEM images (a2, b2 and c2) of $Ni(OH)_2$/CMFs/$Ni(OH)_2$ (a1 and a2), NiO/CMFs/NiO (b1 and b2) and Ni_3N/CMFs/Ni_3N (c1 and c2). For NiO/CMFs/NiO, only five characteristic peaks of NiO phase (JCPDS, No. 14-0117) can be seen in its XRD pattern (b1).

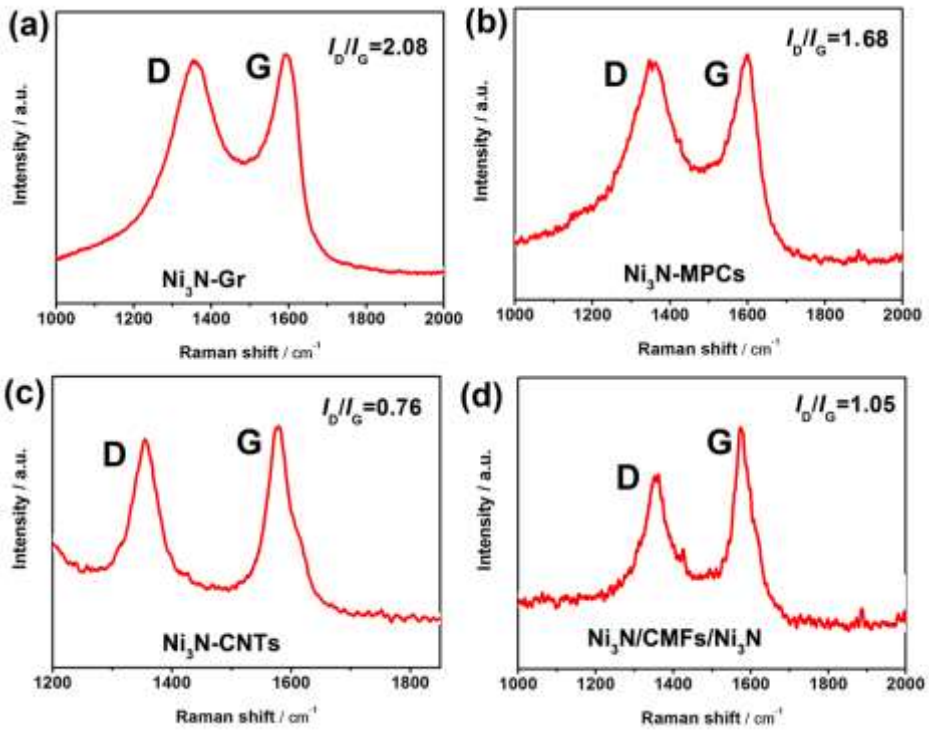

Figure S5 Raman spectra of the resultant Ni_3N-Gr (a), Ni_3N-MPCs (b), Ni_3N-CNTs (c), and Ni_3N/CMFs/Ni_3N (d) hybrid nanomaterials.

Table S1. The comparison of textural properties and Raman analysis results for bulk Ni_3N, Ni_3N-Gr, Ni_3N-MPCs, Ni_3N-CNTs and Ni_3N/CMFs/Ni_3N hybrid materials.

Samples	**S_{BET} ($m^2\ g^{-1}$)**	**Pore Volume ($m^3\ g^{-1}$)**	**Average pore width (nm)**	**I_D/I_G**
Bulk Ni_3N	2.79	0.03	-	-
Ni_3N-Gr	152.45	0.16	6.21	2.08
Ni_3N-MPCs	94.39	0.14	9.36	1.68
Ni_3N-CNTs	67.70	0.21	17.54	0.76
Ni_3N/CMFs/Ni_3N	126.53	0.40	20.86	1.05

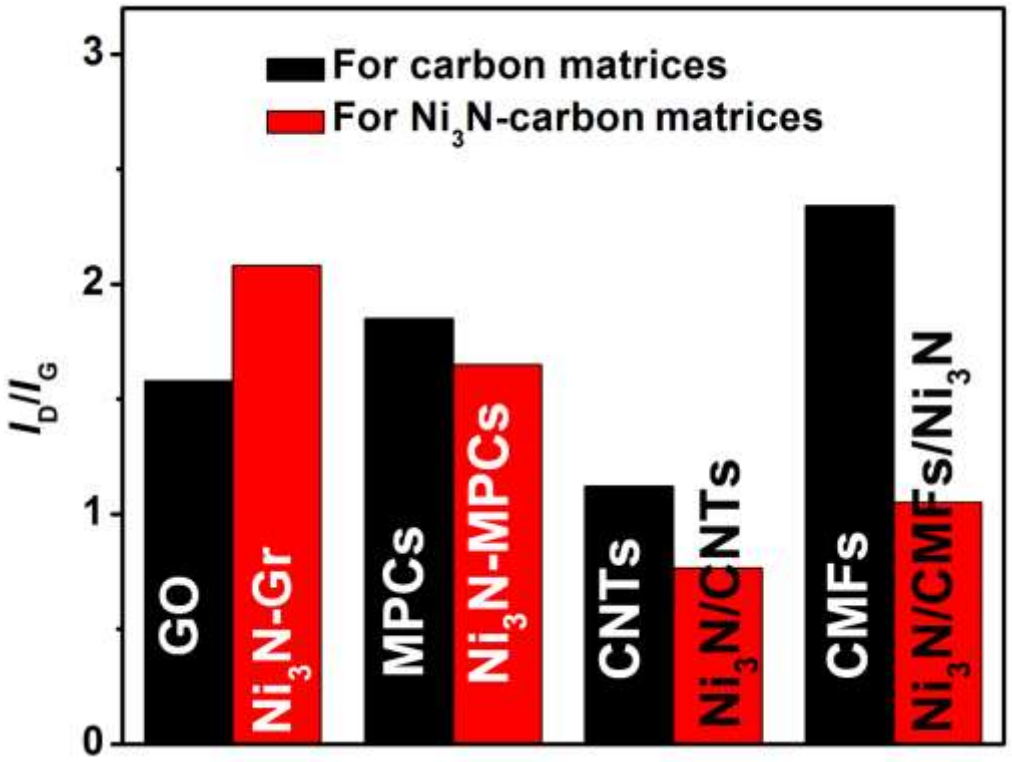

Figure S6 The I_D/I_G values diagram which was obtained from the Raman spectra in **Figures S5** and **S3**.

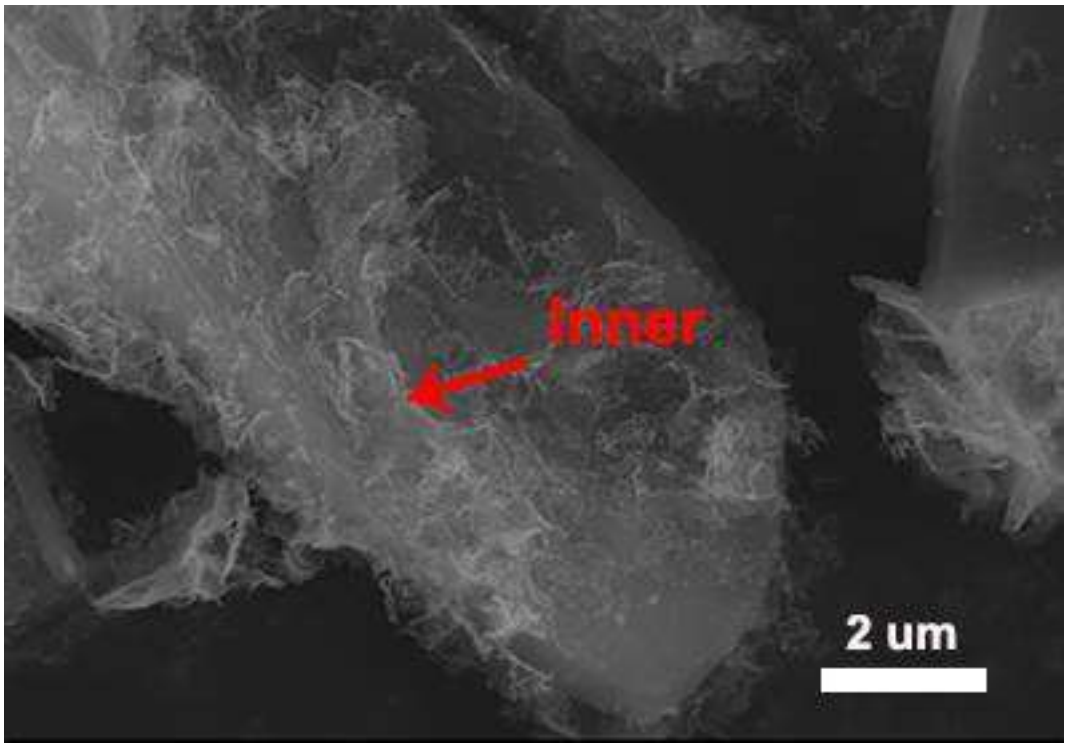

Figure S7 SEM image of the inner wall of as-prepared Ni_3N/CMFs/Ni_3N sample.

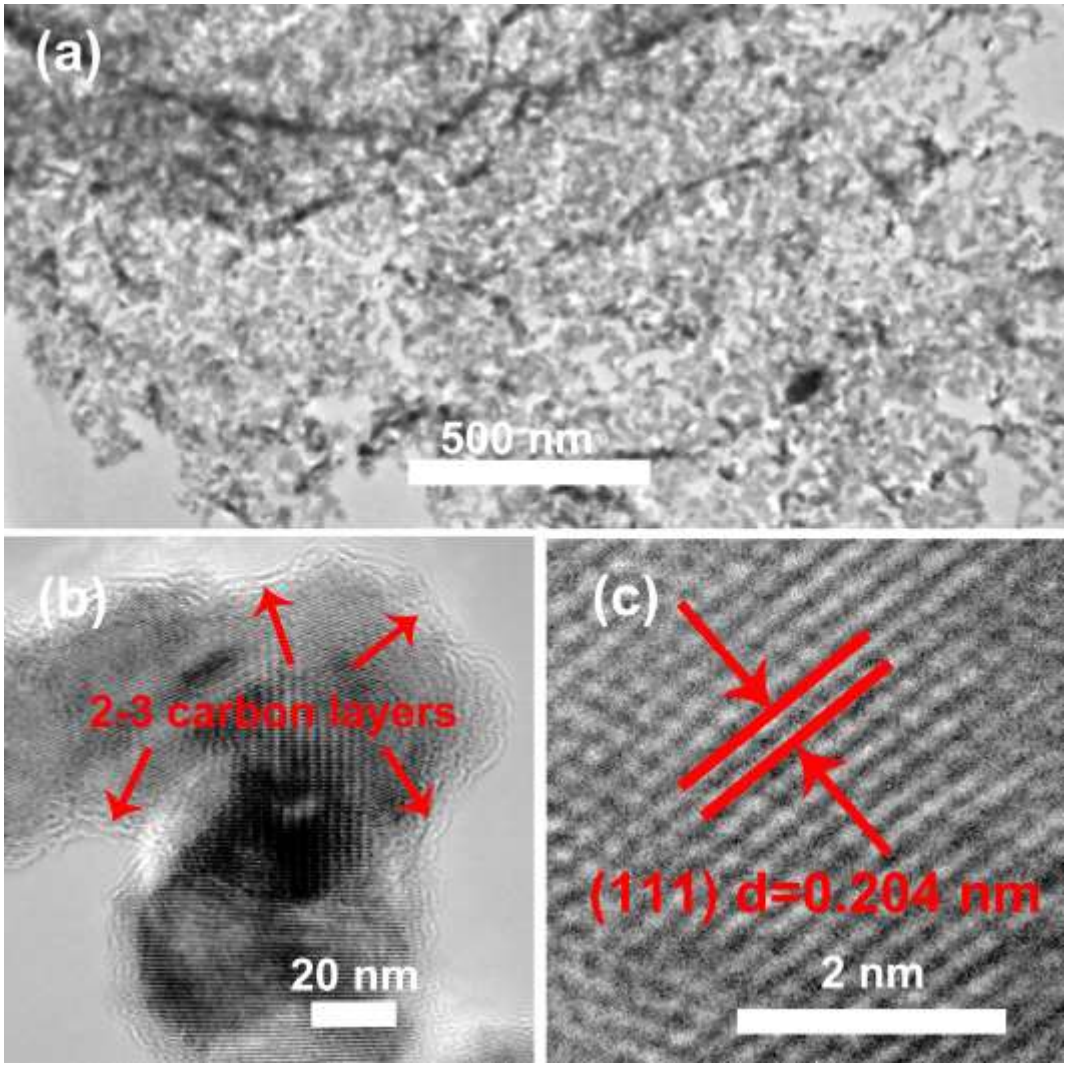

Figure S8 (a) TEM image of an individual Ni_3N NSs located on outer surface of Ni_3N/CMFs/Ni_3N. (b-c) TEM images of the Ni_3N NPs embed in the Ni_3N NSs. As shown, each Ni_3N NPs core showing the polycrystalline structure was surrounded by several carbon shells.

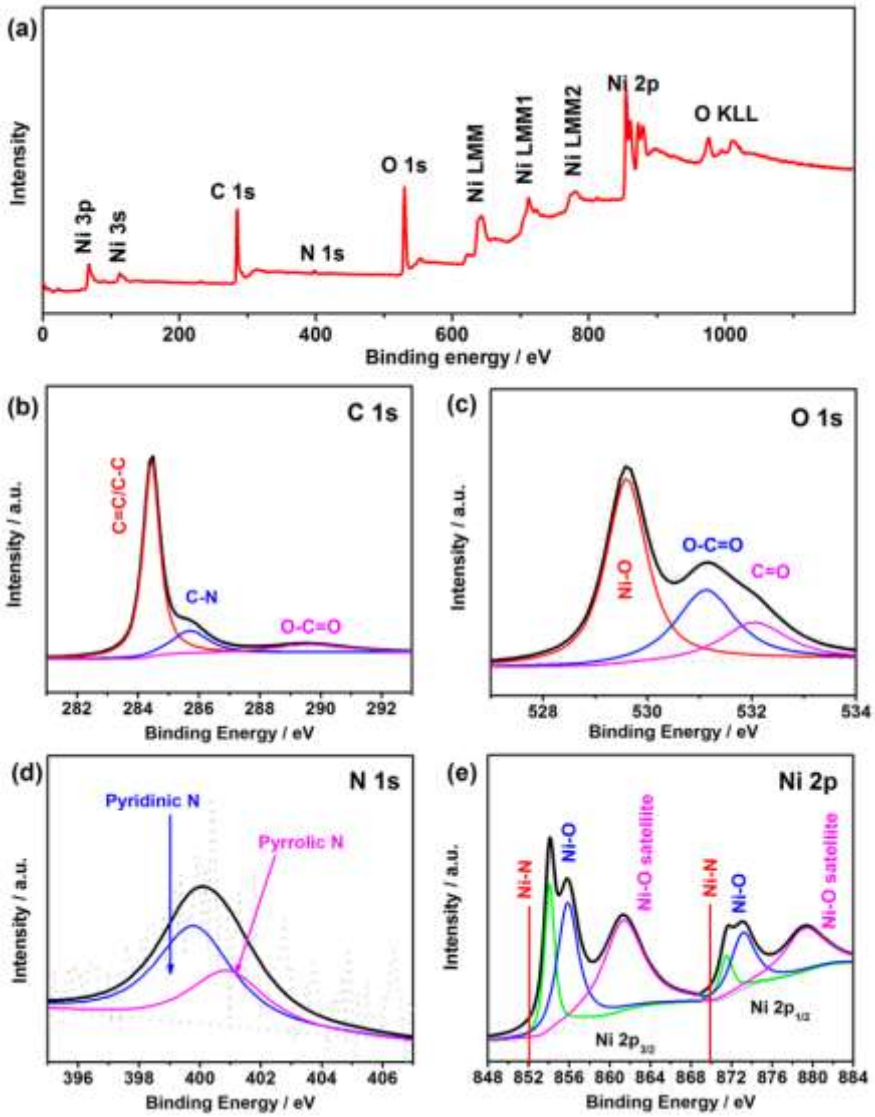

Figure S9 XPS survey spectra (a) and high-resolution XPS spectra of C 1s (b), O 1s (c), N 1s (d), and Ni 2p (e) for the NiO/CMFs/NiO hybrid sample.

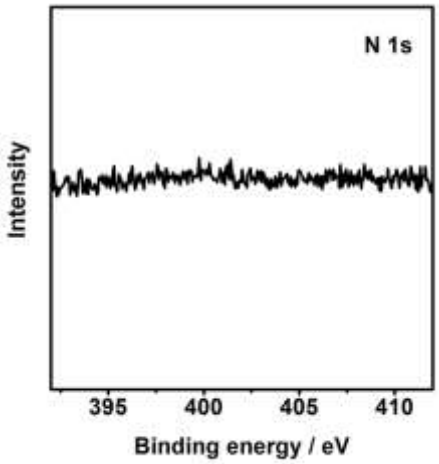

Figure S10 The high-resolution N 1s XPS spectrum of CMFs matrices after being calcined at 400 ^{o}C under NH_3 atmosphere for 2 h.

To verify the OER catalytic efficiency of metallic Ni_3N NSs itself, electrochemical measurements were performed for $Ni(OH)_2$/CMFs/$Ni(OH)_2$ and NiO/CMFs/NiO in 1.0 M KOH (**Figure S11**). As shown in **Figure S11a**, the Ni(II)-to-Ni(III) oxidation potential for Ni_3N/CMFs/Ni_3N is much more negative than that for either $Ni(OH)_2$/CMFs/$Ni(OH)_2$ or NiO/CMFs/NiO, demonstrating the Ni atoms in Ni_3N/CMFs/Ni_3N were much easier to be oxidized to NiOOH with higher valence state compare to $Ni(OH)_2$/CMFs/$Ni(OH)_2$ or NiO/CMFs/NiO. The OER performance derived from LSV curves for Ni_3N/CMFs/Ni_3N (E_{onset} of 1.435 V *vs.* RHE, E_{10} of 1.503 V *vs.* RHE, Tafel slope of 41.54 mV dec^{-1}) was better than those of $Ni(OH)_2$/CMFs/$Ni(OH)_2$ (1.638 V *vs.* RHE, 1.716 V *vs.* RHE, 58.96 mV dec^{-1}) and NiO/CMFs/NiO (1.658 V *vs.* RHE, 1.732 V *vs.* RHE, 65.34 mV dec^{-1}) (**Figures S11b-e**).

On the other hand, the porous structure of the Ni_3N NSs on Ni_3N/CMFs/Ni_3N was able to promote the charge-transfer rate compared with either NiO NSs or $Ni(OH)_2$ NSs with the relatively smooth surface. For this, EIS spectra (**Figure S11f**) of three samples have provided the robust evidence with Ni_3N/CMFs/Ni_3N own the minimum R_{ct} value *versus* the other two reference samples. For the three control samples, as the hollow tube-type structures are shared characteristics, the better catalytic ability of Ni_3N/CMFs/Ni_3N is mainly because of the enhanced metallic electrical conductivity behavior of Ni_3N phase, more exposed active sites of mesoporous Ni_3N NSs, and the higher charge-transfer rate of ultra-thin 2D mesoporous Ni_3N NSs suffering from the etching of NH_3 (**Figure S4c2**).

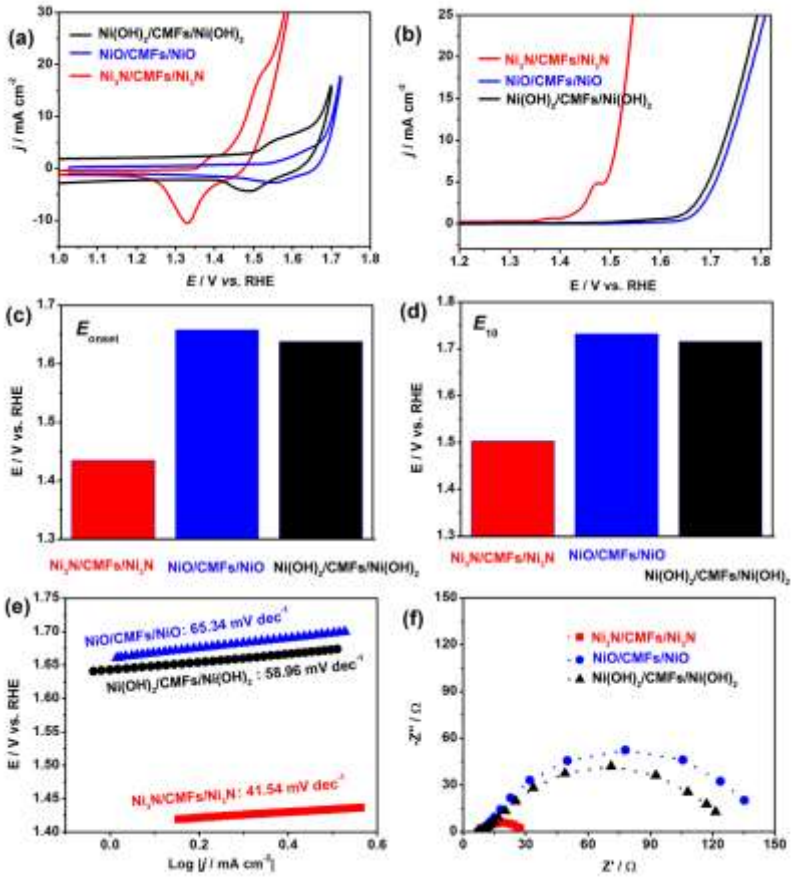

Figure S11 (**a**) CV curves recorded at 50 mV s^{-1} in 1.0 M KOH, **(b)** *IR*-corrected LSV polarization curves for OER collected at 5 mV s^{-1} in O_2-saturated 1.0 M KOH, and the histograms of OER E_{onset} **(c)** and E_{10} (got at a current density of 10 mA cm^{-2}) values **(d)** for Ni_3N/CMFs/Ni_3N, $Ni(OH)_2$/CMFs/$Ni(OH)_2$, and NiO/CMFs/NiO. **(e)** Tafel plots derived from OER LSVs shown in Figure S11b and **(f)** EIS spectra measured at 1.60 V *vs.* RHE for Ni_3N/CMFs/Ni_3N and 1.80 V *vs.* RHE for $Ni(OH)_2$/CMFs/$Ni(OH)_2$ and NiO/CMFs/NiO.

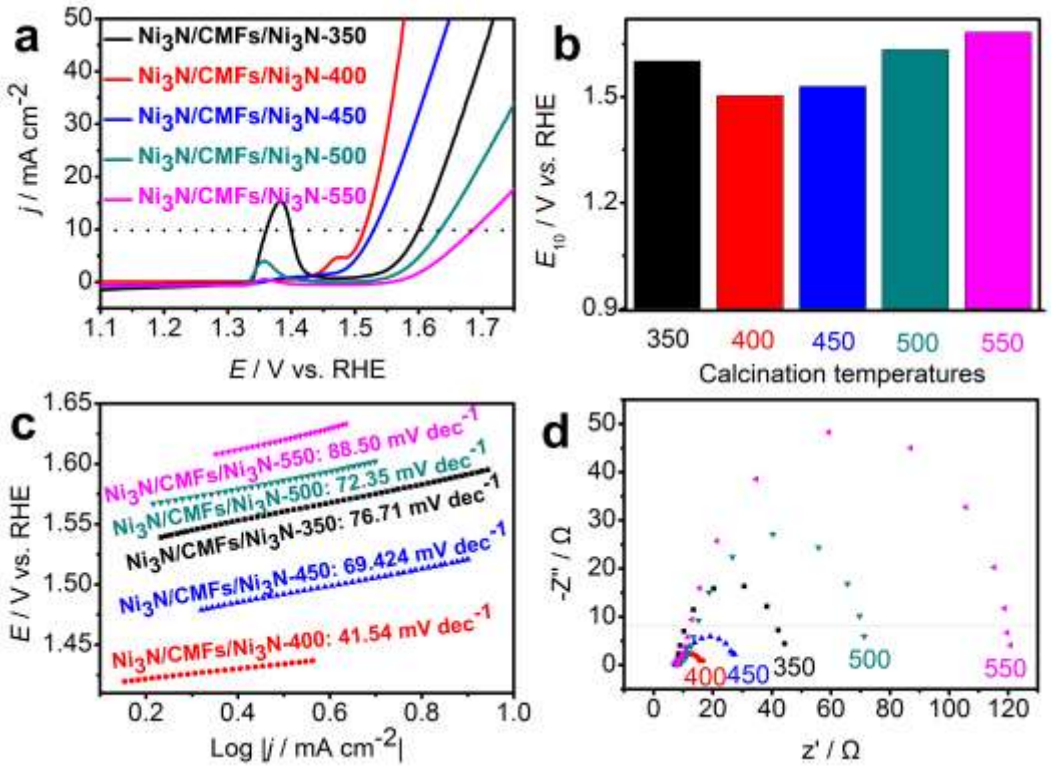

Figure S12 (a) *IR*-corrected LSV polarization curves for OER collected at 5 mV s^{-1}. (b) The histograms of OER E_{10} values. (c) Tafel plots derived from OER LSVs in Figure S12a. (d) EIS spectra measured at 1.60 V *vs.* RHE for Ni_3N/CMFs/Ni_3N-*T* samples calcined at 350, 400, 450, 500, and 550 ^oC.

To verify the OER catalytic efficiencies of Ni_3N/CMFs/Ni_3N-*T* samples calcined at 350, 400, 450, 500, and 550 ^oC, respectively. Electrochemical measurements were performed for Ni_3N/CMFs/Ni_3N-*T* (*T*=350, 400, 450, 500, and 550 ^oC) samples in 1.0 M KOH (**Figure S12**). As shown in **Figures S12a-c**, the E_{10} value (1.503 V *vs.* RHE) and Tafel slope (41.54 mV dec^{-1}) of Ni_3N/CMFs/Ni_3N-400 toward OER are much smaller than those of Ni_3N/CMFs/Ni_3N-350 (E_{10} =1.601 V *vs.* RHE, Tafel slope=76.71 mV dec^{-1}), Ni_3N/CMFs/Ni_3N-450 (E_{10}=1.529 V *vs.* RHE, Tafel slope=69.42 mV dec^{-1}), Ni_3N/CMFs/Ni_3N-500 (E_{10}=1.633 V *vs.* RHE, Tafel slope=72.35 mV dec^{-1}), and Ni_3N/CMFs/Ni_3N-550 (E_{10}=1.683 V *vs.* RHE, Tafel slope=88.50 mV dec^{-1}). At the same time, the R_{ct} values at 1.60 V *vs.* RHE for different Ni_3N/CMFs/Ni_3N-*T* materials increased by the order of Ni_3N/CMFs/Ni_3N-400 < Ni_3N/CMFs/Ni_3N-450 < Ni_3N/CMFs/Ni_3N-350 < Ni_3N/CMFs/Ni_3N-500 < Ni_3N/CMFs/Ni_3N-550. This means that Ni_3N/CMFs/Ni_3N-400 exhibited faster charge-transfer rate in comparison with all other Ni_3N/CMFs/Ni_3N-*T* materials calcined at 350, 450, 500, and 550 ^oC. In conclusion, 400 ^oC is the optimal pyrolysis temperature for synthesizing the most efficient Ni_3N/CMFs/Ni_3N catalyst toward OER.

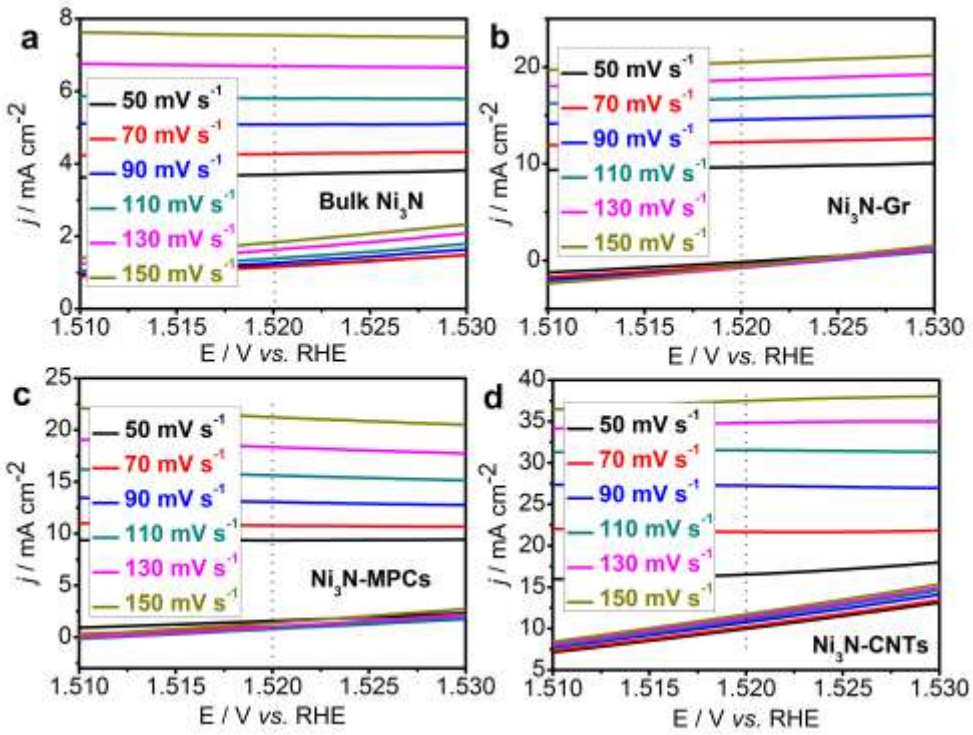

Figure S13 CV curves recorded at different scan rates from 50 to 150 mV s^{-1} between a potential range of 1.51-153 V *vs.* RHE for bulk Ni_3N **(a)**, Ni_3N-Gr **(b)**, Ni_3N-MPCs **(c)**, and Ni_3N-CNTs **(d)** in 1.0 M KOH solution.

Table S2 A comparison on OER catalytic parameters between our resultant catalysts and other as-reported non-precious metal based OER catalysts.

Catalyst	***E* at 10 mA cm^{-2} (V vs. RHE)**	**Tafel slope (mV dec^{-1})**	**References**
Bulk Ni_3N	1.737	66.98	**This work**
Ni_3N-Gr	1.607	58.23	
Ni_3N-MPCs	1.594	57.36	
Ni_3N-CNTs	1.551	50.07	
Ni_3N/CMFs/Ni_3N	**1.503**	**41.54**	
RuO_2	1.534	43.45	
Ni_2P nanowires	1.52	47	Energy Environ. Sci., 2015, 8, 2347-2351
NiSe/NF	1.50	64	Angew.Chem. Int .Ed. 2015, 54,9351 –9355
NiFe@NC	1.58	56	Nano Energy 30 (2016) 426–433
TiN@Ni_3N	1.58	93.7	J. Mater. Chem. A, 2016, 4, 5713–5718
FeNi@NC	1.51	70	Energy Environ. Sci., 2016, 9, 123-129
Ni_3Se_2–GC	1.54	79.5	Energy Environ. Sci., 2016, 9, 1771-1782
MWCNTs@NiCoS	1.59	96	ACS Appl. Mater. Interfaces, 2016, 8 (1), 945
Co_4N	1.56	58	Inorg. Chem. Front., 2016, 3, 236–242

CoN	1.52	70	Angew.Chem. Int. Ed. 2016, 55,8670 –8674
Co_4N nanowire arrays	1.49	44	Angew. Chem. 2015, 127, 14923–14927
Co-B_iNSs/G hybrids	1.52	53	Angew.Chem. 2016, 128,2534–2538
Co@Co_3O_4/NC	1.64	54.3	Angew.Chem. Int.Ed. 2016, 55,4087 –4091
CP/CTs/Co-S	1.536	72	ACS Nano 2016, 10, 2342−2348
Co_3O_4/N-graphene	1.54	67	Nature Materials, 10 (2011) 780-786.
CoP/rGO	1.57	66	Chem. Sci., 2016, 7, 1690–1695
N-CG-CoO	1.57	71	Energy Environ. Sci., 7 (2014) 609-616
CoFe/C	1.53	61	Chem. Sci., 2015, 6, 3572-3576
Co_3O_4/BDHC	1.59	47	Adv. Funct. Mater. 2014, 24, 7655-7665
$CoSe_2$-N-Gr	1.55	44	J. Am. Chem. Soc. 2014, 136, 15670-15675
NCNTs/$Co_xMn_{1-x}O$	1.57	40	Nano Energy (2016) 20, 315–325
CoPi	1.61	58.7	Small, 2016, 12, 1709-1715.
Porous MoO_2 needs	1.49	54	Advanced Materials, 2016, 28(19): 3785-3790.
$LiCoO_2$	1.66	48	EnergyEnviron.Sci., 2016, **9**, 184-192

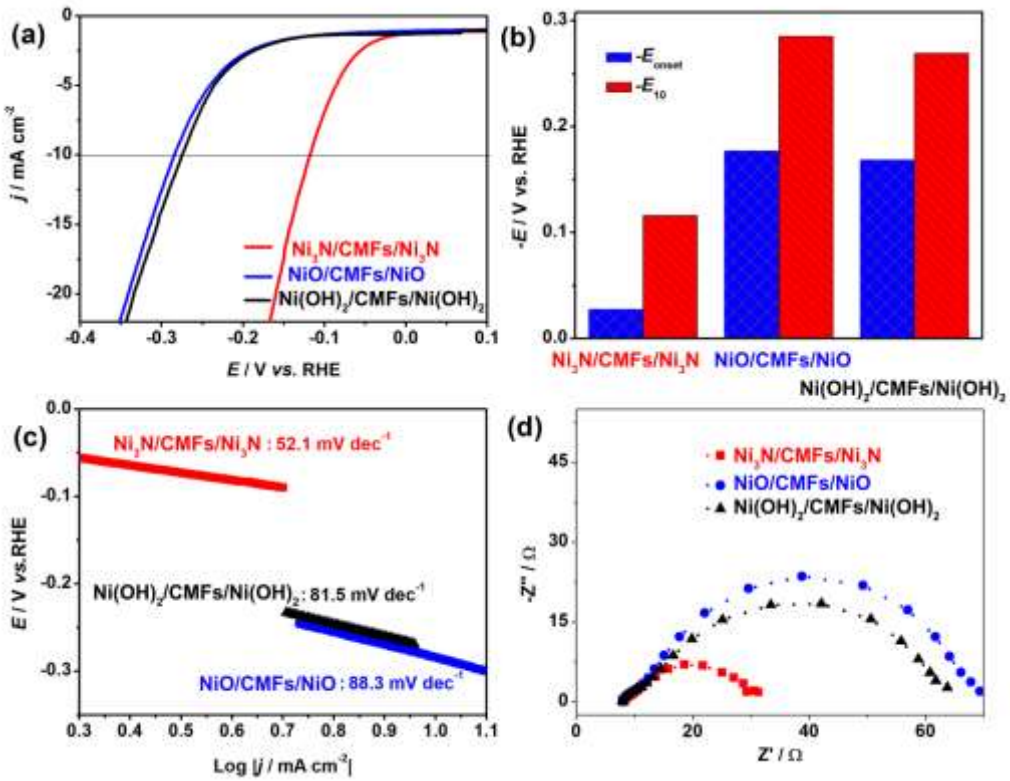

Figure S14 (a) *IR*-corrected LSV polarization curves for HER at 5 mV s^{-1} in N_2-saturated 1 M KOH. (b) The histograms of HER E_{onset} and E_{10} (got at a current density of 10 mA cm^{-2}) values, and (c) Tafel plots derived from HER LSV polarization curves shown in Figure S14a. (d) EIS spectra measured at -0.25 V (*vs.* RHE) for Ni_3N/CMFs/Ni_3N, $Ni(OH)_2$/CMFs/$Ni(OH)_2$, and NiO/CMFs/NiO in N_2-saturated 1 M KOH.

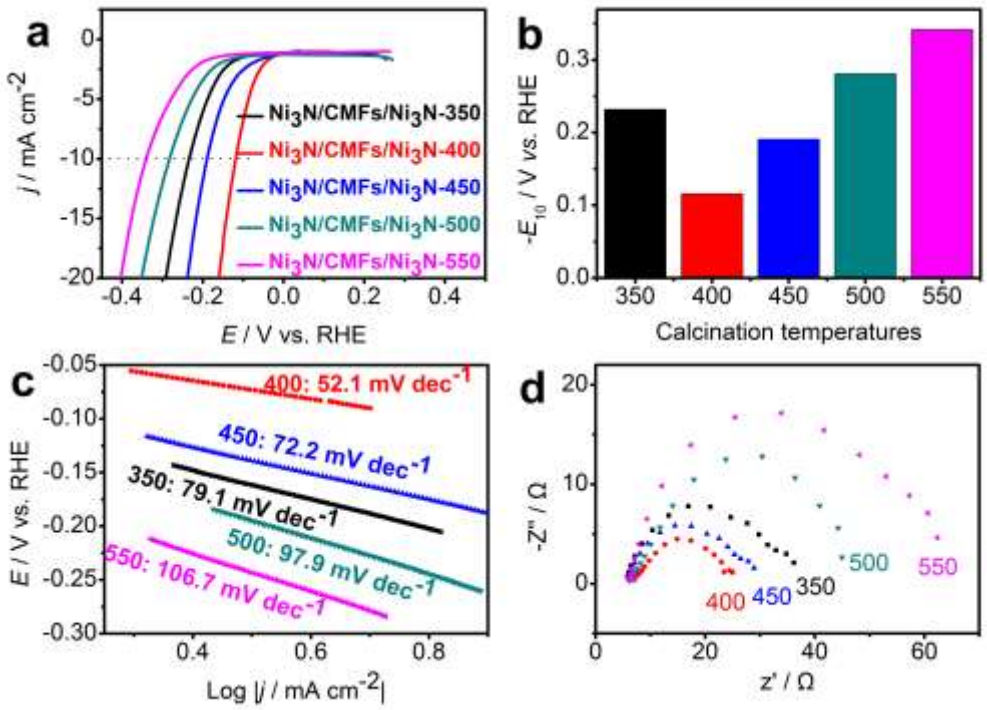

Figure S15 (a) *IR*-corrected LSV polarization curves for HER collected at 5 mV s^{-1}. (b) The histograms of HER E_{10} values. (c) Tafel plots derived from HER LSVs in Figure S15a. (d) EIS spectra measured at -0.25 V *vs.* RHE for Ni_3N/CMFs/Ni_3N calcined at 350, 400, 450, 500, and 550 ^oC.

To verify the HER catalytic efficiencies of Ni_3N/CMFs/Ni_3N-*T* samples calcined at 350, 400, 450, 500, and 550 ^oC, electrochemical measurements were performed for Ni_3N/CMFs/Ni_3N-*T* (*T*=350, 400, 450, 500, and 550 ^oC) samples in 1.0 M KOH (**Figure S15**). As shown in **Figures S15a-c**, the overpotential at 10 mA cm^{-2} (η_{10}: 0.115 V) and Tafel slope (52.1 mV dec^{-1}) of Ni_3N/CMFs/Ni_3N-400 toward HER are much smaller than those of Ni_3N/CMFs/Ni_3N-350 (η_{10} of 0.232 V, Tafel slope of 79.1 mV dec^{-1}), Ni_3N/CMFs/Ni_3N-450 (η_{10} of 0.191 V, Tafel slope of 72.2 mV dec^{-1}), Ni_3N/CMFs/Ni_3N-500 (η_{10} of 0.281 V, Tafel slope of 97.9 mV dec^{-1}), and Ni_3N/CMFs/Ni_3N-550 (η_{10} of 0.342 V, Tafel slope of 106.7 mV dec^{-1}). At the same time, the R_{ct} values at -0.25 V *vs.* RHE for different Ni_3N/CMFs/Ni_3N-*T* materials increase by the order of Ni_3N/CMFs/Ni_3N-400 < Ni_3N/CMFs/Ni_3N-450 < Ni_3N/CMFs/Ni_3N-350 < Ni_3N/CMFs/Ni_3N-500 < Ni_3N/CMFs/Ni_3N-550, which proves that Ni_3N/CMFs/Ni_3N-400 exhibited faster charge-transfer rates in comparison with all other Ni_3N/CMFs/Ni_3N-*T* materials calcined at 350, 450, 500, and 550 ^oC. In conclusion, 400 ^oC is the optimal pyrolysis temperature for synthesizing the most efficient Ni_3N/CMFs/Ni_3N catalyst toward HER.

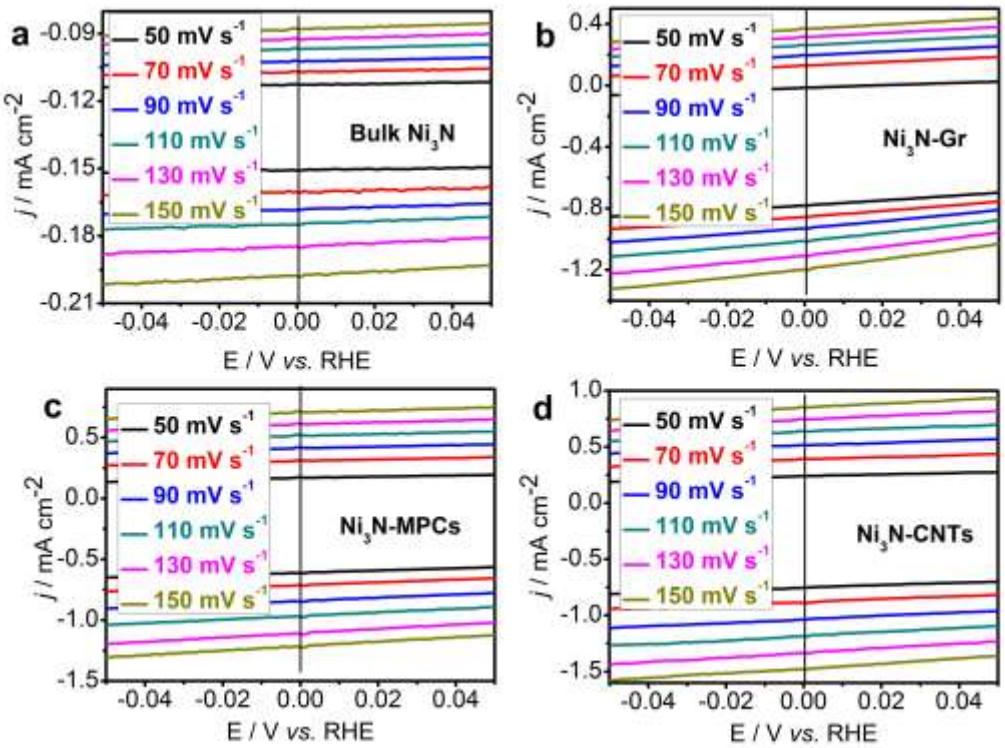

Figure S16 CV curves recorded at different scan rates from 50 to 150 mV s^{-1} between a potential range of -0.05-0.05 V *vs.* RHE for bulk Ni_3N **(a)**, Ni_3N-Gr **(b)**, Ni_3N-MPCs **(c)**, and Ni_3N-CNTs **(d)** in 1 M KOH solution.

Table S3 Comparison of HER activity for those resultant catalysts and other reported non-precious metal based HER catalysts in 1 M KOH.

Catalysts	**E_{10} (V *vs.* RHE)**	**Tafel slopes (mV dec^{-1})**	**References**
Bulk Ni_3N	-0.349	109.2	**This work**
Ni_3N-Gr	-0.201	89.9	
Ni_3N-MPCs	-0.175	74.9	
Ni_3N-CNTs	-0.149	62.5	
Ni_3N/CMFs/Ni_3N	**-0.115**	**52.1**	
Pt/C	**-0.075**	**34.9**	
Ni-NiO/N-rGO	-0.26	67	Adv. Funct. Mater. 2015, 25, 5799–5808
Ni_2P Nanosheets	-0.078	142	ACS Appl. Mater. Interfaces, 2015, 7 (4), 2376-2384
Ni_2P	-0.25	100	J Am Chem Soc 2013, 135(51): 19186-19192
Ni_5P_4	-0.15	53	Angew.Chem.Int. Ed. 2015, 127,12538-12542
NiSe/NF	-0.096	120	Angew.Chem.Int. Ed. 2015, 54,9351-9355
$NiFeO_x$/CFP	-0.088	84.6	Nature Communications 2015, 6, 7261
EG/$Co_{0.85}$Se/NiFe-LDH	-0.26	160	Energy Environ. Sci., 2016, **9**, 478-483
Ni-B_x film	-0.135	88	Nano Energy (2016) 19, 98-107
$Co_{0.6}Mo_{1.4}N_2$	-0.32	80	Nat Mater 2012, 11(6): 550-557
Co@CNF	-0.196	96	Nano Energy 23 (2016) 105–113

$Zn_{0.30}Co_{2.70}S_4$	-0.085	47.5-	J. Am. Chem. Soc. 2016, 138, 1359−1365
ONPPGC/OCC	-0.446	154	Energy Environ. Sci., 2016, 9, 1210-1214
CoP/rGO-400	-0.15	38	Chem. Sci., 2016, **7**, 1690-1695
Ni-Mo-N	-0.043	40	Nano Energy (2016) 22, 111–119
CoS_2 MW	-0.158	58	J. Am. Chem. Soc. 2014, 136, 10053−10061
MoS_{2+x}–CE	-0.31	84	Angew. Chem. Int. Ed. 2015, 54, 664 –667
CP/CTs/Co-S	-0.19	131	ACS Nano 2016, 10, 2342−2348
CoPS NPl	-0.048	56	
P-1T-MoS_2	-0.153	43	J. Am. Chem. Soc. 2016, 138, 7965−7972

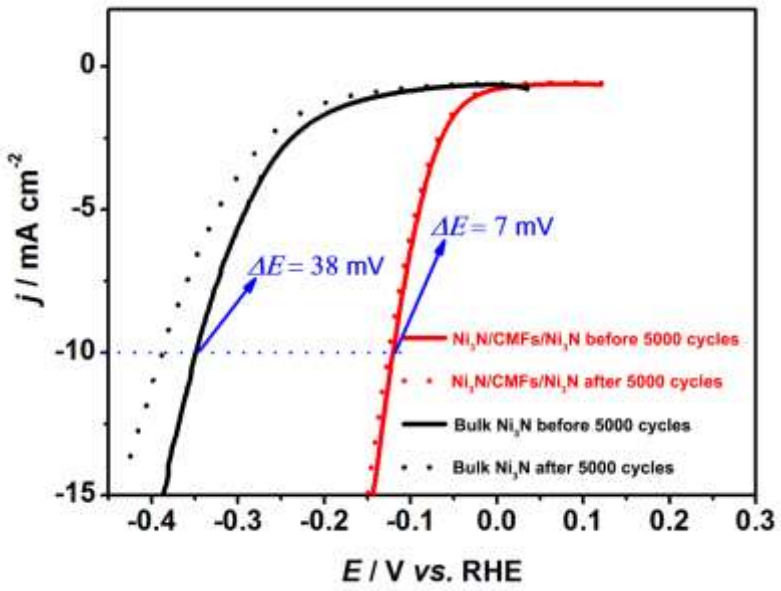

Figure S17 HER stability tests for the bulk Ni_3N and Ni_3N/CMFs/Ni_3N, by comparing their LSV polarization curves before and after 5000 CV cycles [cycling between -0.35 and 0.10 V (vs. RHE)].

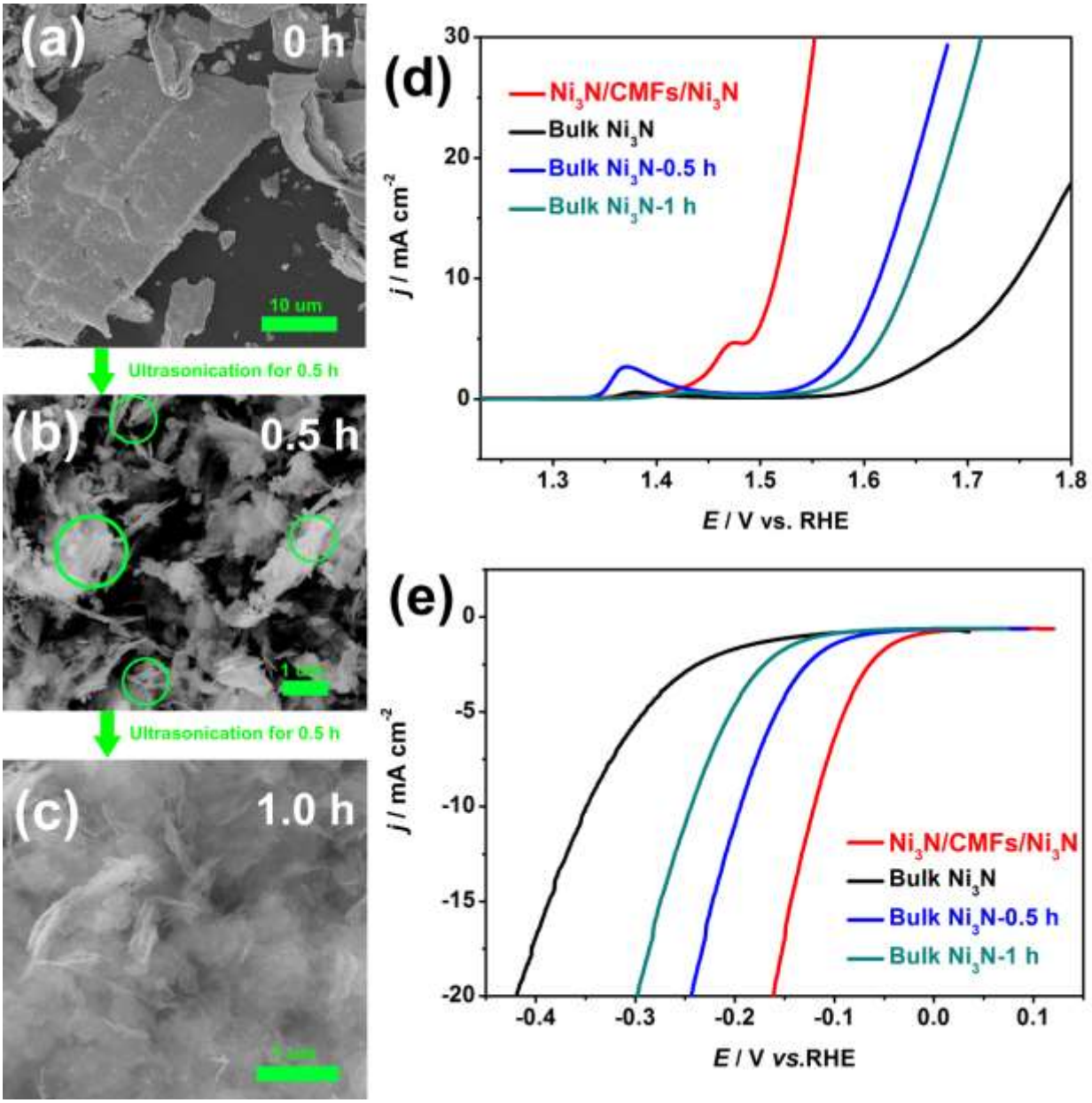

Figure S18 SEM images of (a) the initial bulk Ni_3N, (b) the bulk Ni_3N after the ultrasonication treatment for 0.5 h (denoted as Ni_3N-0.5), and (c) the bulk Ni_3N after the ultrasonication treatment for 1 h (denoted as Ni_3N-1). (d) *IR*-corrected LSV polarization curves for OER in O_2-saturated 1.0 M KOH at 5 mV s^{-1} and (e) *IR*-corrected LSV polarization curves for HER in N_2-saturated 1 M KOH at 5 mV s^{-1} for the bulk Ni_3N, Ni_3N-0.5, Ni_3N-1, and Ni_3N/CMFs/Ni_3N.

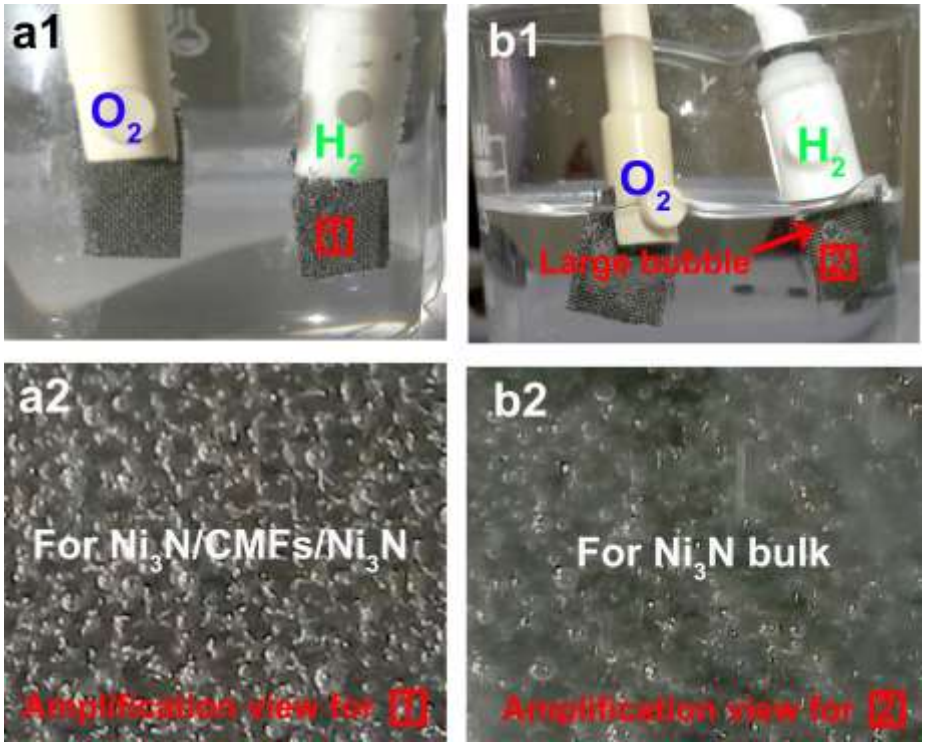

Figure S19 The digital graphs of the processes in full water splitting of Ni_3N/CMFs/Ni_3N (a1-a2) and bulk Ni_3N (b1-b2). The applied current densities are all 10 mA cm^{-2}.

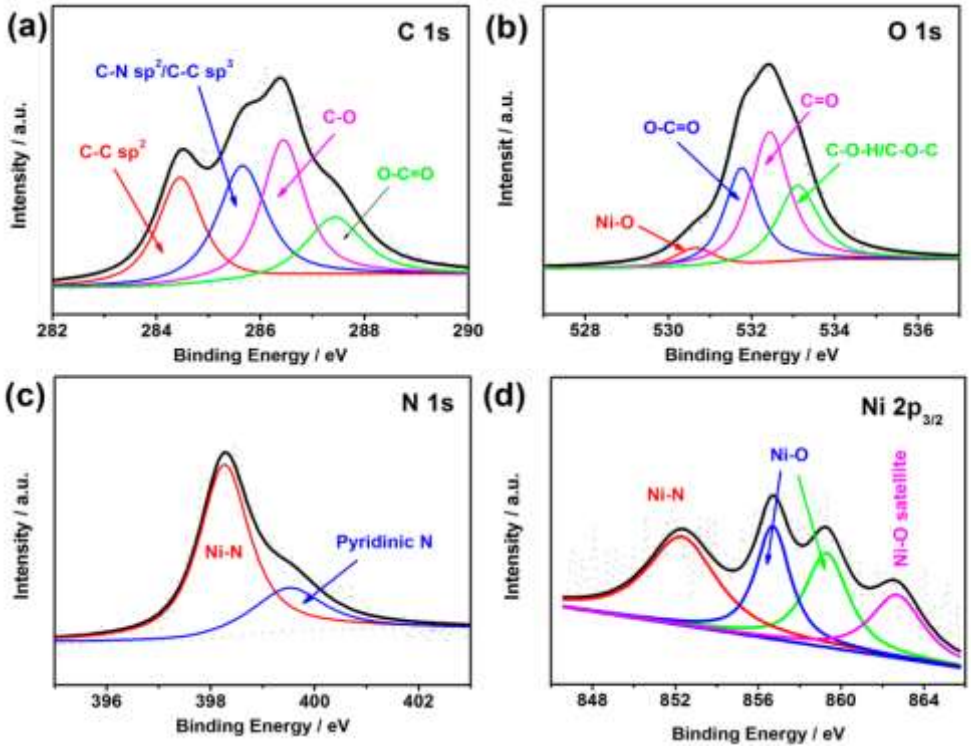

Figure S20 High-resolution XPS spectra of C 1s (a), O 1s (b), N 1s (c), and Ni 2p (d) for the post-OER Ni_3N/CMFs/Ni_3N.

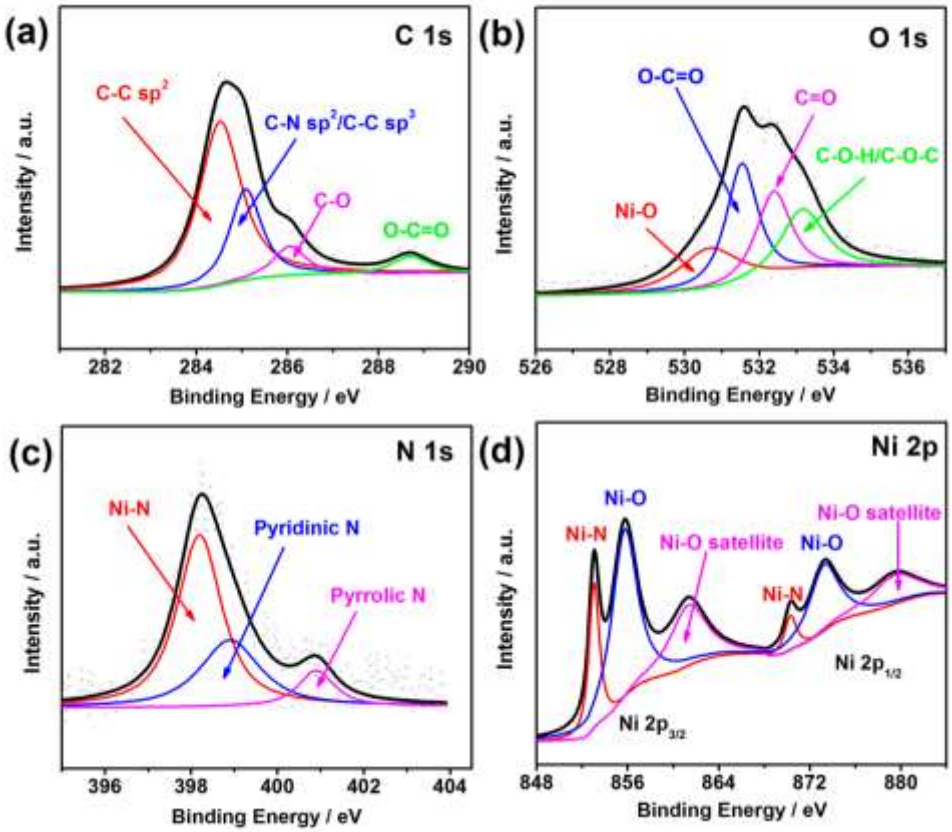

Figure S21 High-resolution XPS spectra of C 1s (a), O 1s (b), N 1s (c), and Ni 2p (d) for the post-HER Ni_3N/CMFs/Ni_3N.

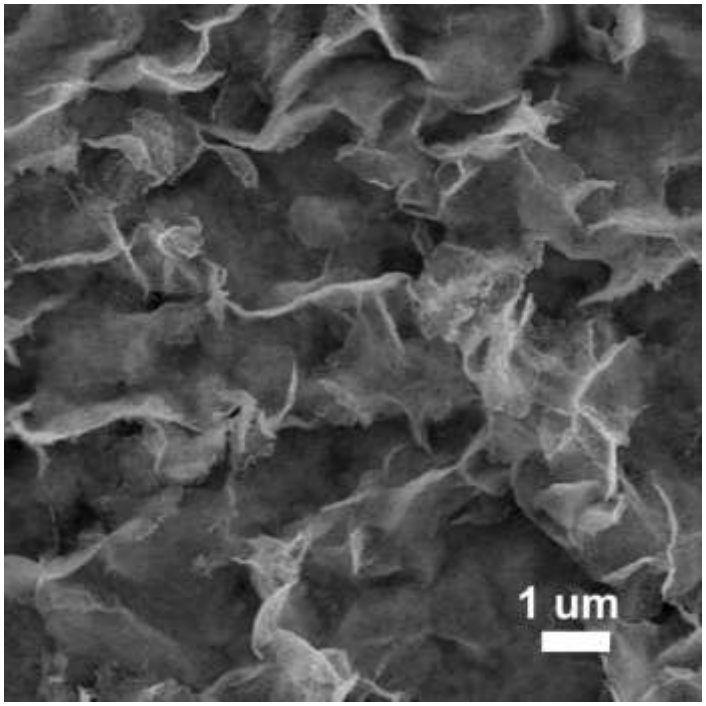

Figure S22 SEM image of the post-OER Ni_3N/CMFs/Ni_3N collected at positive electrode after the 40 h of water splitting catalysis.

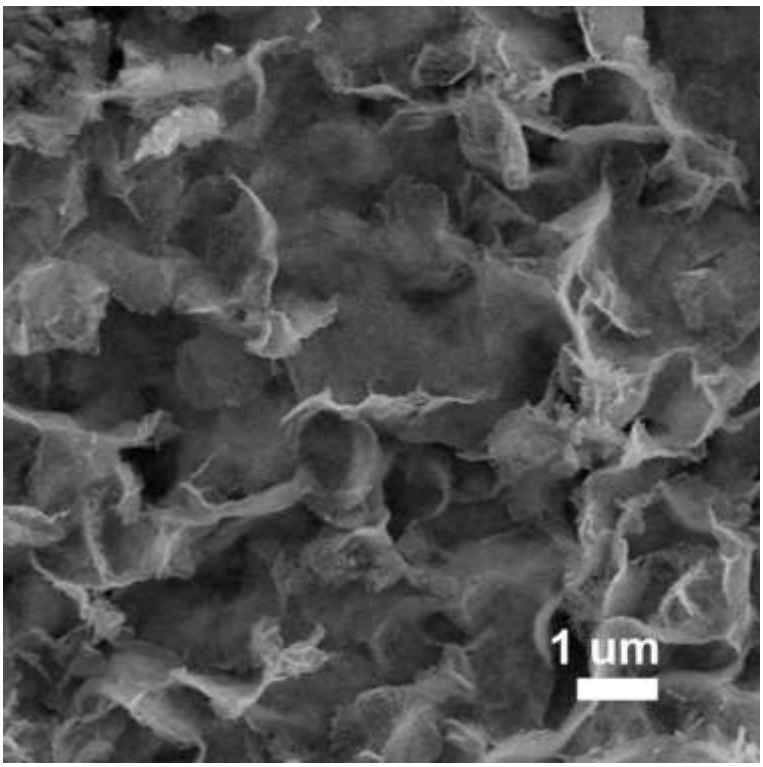

Figure S23 SEM image of the post-HER Ni_3N/CMFs/Ni_3N collected at negative electrode after the 40 h of water splitting catalysis.

References:

1. W. S. Hummers and R. E. Offeman, Journal of the American Chemical Society, 1958, 80, 1339-1339.

2. L. Yan, X. Bo, Y. Zhang and L. Guo, Electrochimica Acta, 2014, 137, 693-699.

3. M. Li, Y. Xiong, X. Liu, C. Han, Y. Zhang, X. Bo and L. Guo, Journal of Materials Chemistry A, 2015, 3, 9658-9667.